# Quantum anomalous Hall effect in perfectly compensated collinear antiferromagnetic thin films

Chao Lei [●],[1] Thaís Victa Trevisan,[2,3] Olle Heinonen,[4,*] R. J. McQueeney,[2,3] and A. H. MacDonald[1]

[1]*Department of Physics, The University of Texas at Austin, Austin, Texas 78712, USA*
[2]*Ames Laboratory, Ames, Iowa 50011, USA*
[3]*Department of Physics and Astronomy, Iowa State University, Ames, Iowa 50011, USA*
[4]*Materials Science Division, Argonne National Laboratory, Lemont, Illinois 60439, USA*

We show that the quantum anomalous Hall effect almost always occurs in magnetic topological insulator thin films whenever the top and bottom surface layer magnetizations are parallel at some temperature, independent of the interior layer magnetization configuration. Using this criterion, we identify structures that have a quantum anomalous Hall effect even though they have collinear magnetic structures with no net magnetization, and discuss strategies for realizing these interesting magnetic states experimentally.

## I. INTRODUCTION

The anomalous Hall effect (AHE) was observed [1,2] already in the 19th century, but understood quantitatively only recently [3]. The discovery of the quantum Hall effect [4,5], and its interpretation [6] in terms of momentum space Chern numbers, played a role in improving our understanding of the AHE by clarifying why the intrinsic momentum-space Berry curvature contribution [7], which had sometimes been controversial, can play an important role. For many classes of materials, predictive theories of the AHE that include extrinsic skew scattering [8,9] and side-jump [10] effects along with intrinsic contributions [7] are now available. The theory of the AHE is especially simple in quasi-two-dimensional magnetic insulators, since it is then purely intrinsic and must be quantized.

Historically, the AHE was often assumed to be proportional to the magnetization, and therefore to be a characteristic of ferromagnets, not antiferromagnets. Indeed, rigorous symmetry arguments can be used to rule out an AHE in usual Neél antiferromagnets which have a combined $\mathcal{TO}$ symmetry, where $\mathcal{T}$ is the time-reversal symmetry and $\mathcal{O}$ is a translation that transposes magnetic sublattices [11]. In the presence of this symmetry, the Berry curvature satisfies $\Omega(\mathbf{k}) = -\Omega(-\mathbf{k})$. When inversion symmetry also exists $\Omega(\mathbf{k}) = \Omega(-\mathbf{k})$, this additional condition thus leads to zero Berry curvature everywhere in the Brillouin zone (BZ). However, AHEs are found in both noncollinear [11–18] and collinear [11,19–21] antiferromagnets that do not possess a symmetry of this type. AHEs in antiferromagnets are of technological interest because they provide easy access to information stored in hysteretic antiferromagnetic order configurations.

The property that the Hall conductivity of any two-dimensional band insulator $\sigma_{xy} = \sigma e^2/h$ is quantized was recognized [22] as an outgrowth of the topological theory [6] of the quantum Hall effect [4]. Although the specific model

studied in Ref. [22] is not physically realistic, it demonstrated that nonzero integer values of $\sigma$ could in principle be produced not only by external magnetic fields but also by spontaneous time-reversal symmetry breaking. This quantized version of the AHE (QAHE) was first realized [23] experimentally, in work motivated by a theoretical proposal [24], in magnetically doped and ferromagnetically ordered topological insulators. The QAHE was also recently observed in odd layer number ($N$) thin films of MnBi$_2$Te$_4$ [25–28], which is an A-type antiferromagnet and a magnetic topological insulator in bulk. Because odd $N$ films have a layer of uncompensated spins, they are quasi-2D ferromagnets. Here we predict that the QAHE also occurs in even $N$ magnetic topological insulator (MTI) thin films that have perfectly compensated collinear magnetic order when the top and bottom surface layer magnetizations are parallel, as illustrated in Fig. 1. We further explain how these magnetic configurations can be realized experimentally.

## II. QUALITATIVE QAHE CRITERIA

Mn(Sb$_x$Bi$_{1-x}$)$_2$X$_4$ ($X$ = Se,Te) thin films consist of van der Waals coupled septuple layers with ferromagnetically ordered Mn local moments at their centers, and perpendicular-to-plane easy axes [29–33]. The ferromagnetic layers are coupled via weak antiferromagnetic exchange interactions that act across the van der Waals gap. This interesting family of materials has recently attracted both theoretical and experimental interest [25,26,28–61]. QAHEs are expected to be common in odd $N$ uncompensated films, and have been observed in MBT (MnBi$_2$Te$_4$) thin film with $N = 5$. [28] QAHEs have also been observed at other film thicknesses [28,41,49] when the magnetic configurations is altered by applying magnetic fields larger than ≈5 T. Compensated antiferromagnetic states with equal numbers of ↑ and ↓ layers are possible for even layer number $N$. The number of compensated magnetic configurations is $C(N, N/2) = 2, 6, 20 \ldots$ for $N = 2, 4, 6 \ldots$. Each of these configurations has a time-reversed partner whose Chern number differs by a sign. Choosing one member

———————
*Present address: Seagate Technology, 7801 Computer Avenue, Bloomington, MN 55435.
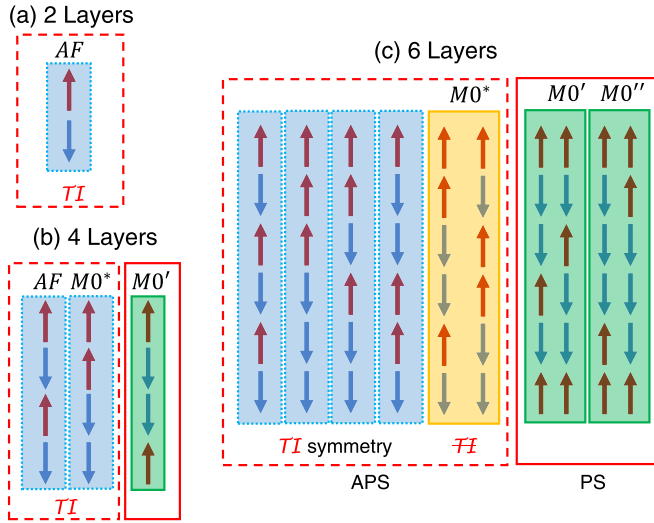
FIG. 1. Fully compensated magnetic configurations of two-, four-, and six-layer MTI thin films. Only configurations that are distinct under global spin reversal are illustrated. Odd parity configurations (blue) yield a band Hamiltonian with $\mathcal{TI}$ symmetry and necessarily have Hall quantum integer $\sigma = 0$. We find that configurations that are not odd parity, but still have antiparallel surface (APS) layers (orange) almost always have $\sigma = 0$, while those with parallel surface (PS) layers (green) almost always have $\sigma \neq 0$.

from each time-reversed pair leaves the $C(N, N/2)/2$ configurations illustrated for $N = 2, 4, 6$ in Fig. 1 to be studied.

In this work, we focus on compensated antiferromagnetic states. Our analysis of MTI thin films is based on a simplified coupled Dirac cone model [26] applicable to the $\text{Mn}(\text{Sb}_x\text{Bi}_{1-x})X_4$ ($X = \text{Se,Te}$) family of intrinsic magnetic topological insulators (IMTIs), and on a symmetry analysis of all the possible magnetic configurations to identify cases where the anomalous Hall conductivity is allowed to be finite. We classify the magnetic configurations of even $N$ compensated moment MTI thin films as having either antiparallel surface (APS) layer magnetizations or parallel surface (PS) layer magnetizations as illustrated in Fig. 1. For large and even $N$, the number of PS configurations is almost equal to the

number of APS configurations, as shown in the Appendix A, Fig. 6.

Many APS films have odd-parity magnetization configurations [$2^{N/2}/2$ of the $C(N, N/2)/2$] in the sense that their magnetizations are reversed when the layer order is reversed (blue set in Fig. 1). Even and odd parity magnetic states have distinct symmetries. A single septuple layer (SL) in the paramagnetic state inherits the point group $\bar{3}m1'$ of bulk MBT. This group is generated by a threefold rotation around the stacking direction $\hat{z}$ ($C_{3z}$), a twofold rotation around $\hat{x}$ ($C_{2x}$), where $\hat{x}$ is aligned with one of the in-plane crystallographic axes, spatial inversion ($\mathcal{I}$), and time-reversal ($\mathcal{T}$). When the Mn moments order, some symmetries (e.g., time-reversal symmetry) are broken but in thin films new symmetries can emerge. The four magnetic point groups that can occur in an $N$-layer system are summarized in Table I.

The transformations of the Berry curvature under symmetry operations place constraints on the the Hall conductivity $\sigma_{xy}$. For example, under combined time-reversal and inversion, $\mathcal{TI}$, $\Omega(k_x, k_y) = -\Omega(k_x, k_y)$, forcing $\Omega(k_x, k_y)$ and therefore $\sigma_{xy}$ to vanish identically if $\mathcal{TI}$ is a symmetry of the system. The simplified Dirac model Hamiltonians used below to represent even MBT thin films which have $\mathcal{TI}$ symmetry when the magnetic configuration is odd [62]. In Table I we show that reversed (odd) magnetic configurations do indeed have $\mathcal{TI}$ symmetry, and that no other symmetry of the allowed magnetic point groups forces $\Omega(k_x, k_y)$ to vanish identically or to integrate to zero over the first BZ. Therefore, all even or odd layer magnetic configurations with magnetic point groups that do not contain $\mathcal{TI}$ may admit a finite AHE, and do so when the Fermi level is not in a gap, as shown in the Appendix B, Fig. 10. We find numerically, however, within our low-energy model, that many APS films that do not have $\mathcal{TI}$ symmetry (orange in Fig. 1) still have $\sigma = 0$ when the Fermi level is in the gap. In fact, their Hall conductivities are quantized at zero when insulating. On the other hand, PS magnetic configurations (green in Fig. 1) often have $\sigma \neq 0$, even though their moments are perfectly compensated.

We start by examining the $N = 2$, $N = 4$, and $N = 6$ cases in detail. $C(N, N/2)/2 = 1$ for $N = 2$, leaving one configuration to be studied. Since this configuration has odd parity, the mean-field Hamiltonian has $\mathcal{TI}$ symmetry and we know with-

TABLE I. Magnetic point group (MPG) of the $N$ layer MTI thin films. Reverse (palindrome) magnetic configuration means that their magnetic moments are reversed (identical) when the layer order is reversed. $C_{n\hat{r}}$ denotes a $2\pi/n$ rotation around $\hat{r}$, while $\mathcal{I}$ and $\mathcal{T}$ stand for spatial inversion and time reversal, respectively. $M_x = \mathcal{I}C_{2x}$ denotes the mirror operation that reverses the spatial coordinate $x$ while keeping $y$ and $z$ unchanged. Four distinct MPGs emerges from all the possible magnetic configurations of the layered systems. Other than $\mathcal{TI}$, none of the symmetries that we encounter here constrain the Berry curvature either to identically vanish or to integrate to zero within the BZ, which allows a finite value for the anomalous Hall conductivity in the MPGs where $\mathcal{TI}$ is absent. Note that the anomalous Hall conductivity is typically finite in odd $N$ layer films since $\mathcal{TI}$ is always broken in these systems.

| $N$ | Magnetic order | Generators | MPG | Constraint on $\Omega(\mathbf{k})$ |
|---|---|---|---|---|
| Even | Paramagnetic | $C_{3z}, C_{2x}, \mathcal{I}, \mathcal{T}$ | $\bar{3}m1'$ | $\Omega(\mathbf{k}) = 0$ |
| | Reversed (odd) configuration (e.g., u-d-u-d) | $C_{3z}, C_{2x}, \mathcal{TI}$ | $\bar{3}'m'$ | $\Omega(\mathbf{k}) = 0$ |
| | Palindrome configuration (e.g., u-d-d-u) | $C_{3z}, \mathcal{I}, \mathcal{T}C_{2x}$ | $\bar{3}m'$ | $\int_{\mathbf{k}} \Omega(\mathbf{k}) \neq 0$ |
| | None of the above | $C_{3z}, \mathcal{T}M_x$ | $3m'$ | $\int_{\mathbf{k}} \Omega(\mathbf{k}) \neq 0$ |
| Odd | Paramagnetic | $C_{3z}, C_{2x}, \mathcal{I}, \mathcal{T}$ | $\bar{3}m1'$ | $\Omega(\mathbf{k}) = 0$ |
| | Palindrome configuration (e.g., u-d-u) | $C_{3z}, \mathcal{I}, \mathcal{T}C_{2x}$ | $\bar{3}m'$ | $\int_{\mathbf{k}} \Omega(\mathbf{k}) \neq 0$ |
| | None of the above | $C_{3z}, \mathcal{T}M_x$ | $3m'$ | $\int_{\mathbf{k}} \Omega(\mathbf{k}) \neq 0$ |

out calculation that Berry curvature vanishes and $\sigma = 0$. The thinnest PS configuration occurs at $N = 4$. The three configurations of $N = 4$ thin film in Fig. 1(b) are labeled $AF$, $M0^*$, and $M0'$. Among these only the $M0'$ ($\uparrow\downarrow\downarrow\uparrow$) state has PS configuration and thus can host a QAHE state. For $N = 6$, four of the ten illustrated configurations have $\mathcal{TI}$ symmetry and thus zero Berry curvature and $\sigma = 0$. To determine whether or not the two remaining APS magnetic configurations (denoted as $M0^*$) and the four PS configurations (denoted as $M0'$ and $M0''$) in Fig. 1(c) support QAHE states, it is necessary to examine the electronic structure more closely.

## III. MODEL CALCULATIONS

We employ a low-energy phenomenological band model, discussed in detail in [26], with Dirac cones on both surfaces of each septuple layer:

$$H = \sum_{\mathbf{k}_\perp, ij} [((-)^i \hbar v_D (\hat{z} \times \sigma) \cdot \mathbf{k}_\perp + m_i \sigma_z) \delta_{ij}$$
$$+ \Delta_{ij} (1 - \delta_{ij})] c^\dagger_{\mathbf{k}_\perp i} c_{\mathbf{k}_\perp j}. \quad (1)$$

Here $i$ and $j$ are Dirac cone labels with even integers reserved for septuple layer bottoms and odd for layer tops, $\hbar$ is the reduced Planck constant, $v_D$ is the velocity of the Dirac cones, and $\Delta_{ij}$ is the hopping amplitude between the $i$th and $j$th Dirac cones. Only the four largest model parameters, estimated by fitting to DFT calculations, are retained in our calculations: Hopping between the surface Dirac cones in the same layer ($\Delta_S$), nearest-neighbor hopping between adjacent layers ($\Delta_D$), and two exchange splitting parameters. The exchange splitting parameter $m_i \equiv \sum_\alpha J_{i\alpha} M_\alpha$, where $\alpha$ is a layer label and $M_\alpha = \pm 1$ specifies the direction of magnetization on layer $\alpha$. We define $J_S$ as exchange splitting from the magnetization within the same septuple layer and $J_D$ as the near-neighbor exchange splitting from the magnetism in the adjacent septuple layer. More details can be found in Ref. [26].

Figure 2 contains two-dimensional $|\Delta_D|/\Delta_S$-$J_S/\Delta_S$ topological phase diagrams calculated with $\delta \equiv J_D/J_S = 0.8$, its MBT value [26]. The phases are obtained by tracking band crossings, which always occur at $\mathbf{k}_\perp = \mathbf{0}$, and by explicitly evaluating the Chern numbers numerically on a coarse mesh in parameter space. This figure shows phase diagrams for several fully compensated PS magnetic configurations: Four-layer $M0'$, six-layer $M0'$ and $M0''$, and eight-layer $M0'''$. The phases are identified by explicitly calculating Chern numbers within all distinct regions that are bounded by level crossing lines. In the phase diagrams, light green regions represent quantum anomalous Hall states with Chern number $C = 1$, the dark green regions represent $C = 2$, and the gray regions represent trivial insulators. Quantum anomalous Hall (QAH) states are common in the bottom right regions of these phase diagrams, where $\Delta_D$ is large enough to yield TI states in the absence of magnetism and $J_S$ is small enough that the exchange fields perturb the nonmagnetic TI state weakly. The model parameters estimated for MBT are close to the phase boundaries between QAH and trivial states because the exchange interactions are relatively weak and because these materials are barely topo-
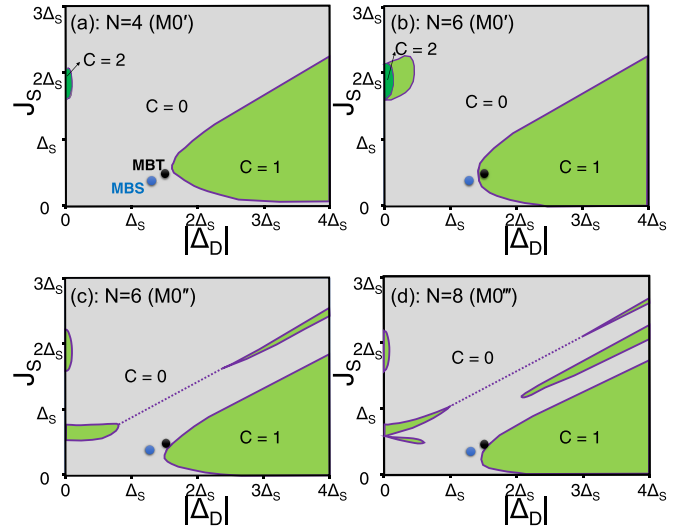


FIG. 2. MTI thin film phase diagrams for a variety of fully compensated PS magnetic configurations. The $x$ and $y$ axes are the ratio of the interlayer to intralayer hybridization $|\Delta_D|/\Delta_S$ and the ratio of exchange and hybridization parameters $J_S/\Delta_S$. $\delta \equiv J_D/J_S$ is fixed at 0.8, the value estimated for MBT. Phase diagrams for larger and smaller values of $\delta$ are included in the Appendix B, Fig. 9. (a) $N = 4$ $M0'$ state; (b) $N = 6$ $M0'$ and (c) $N = 6$ $M0''$ state; (d) $N = 8$ $M0'''$ state with magnetic configuration ($\uparrow\downarrow\downarrow\downarrow\downarrow\uparrow\uparrow\uparrow$). The light green regions of the phase diagram have Chern number magnitude $|C| = 1$, whereas the dark green regions have $|C| = 2$ and the grey regions $C = 0$. Model parameters estimated for MnBi$_2$Se$_4$ and MnBi$_2$Te$_4$ at temperature $T = 0$ are marked by blue and black dots respectively. The dashed lines label gap closures that are not accompanied by topological phase transitions.

logical in the sense [26] that $|\Delta_D/\Delta_S|$ is not much larger than 1.

It is instructive to examine the $J_S = 0$ and $\Delta_D = 0$ lines in the phase diagrams more closely. We do this in Fig. 3 by plotting thin film energy gaps vs $\Delta_D$ at $J_S = 0$ and vs $J_S$ at $\Delta_D = 0$. In Fig. 3(a) we see that large values of $\Delta_D$ increasingly isolate the top and bottom surface Dirac cones of the MBT thin films and decrease the amplitude for tunneling between them across the bulk of the film. The surface isolation property at large $\Delta_D$ can be understood qualitatively by examining the bilayer limit of the Dirac cone model, for which the band gap at $J_S = 0$ is $E_g = \sqrt{\Delta_D^2 + 4\Delta_S^2} - |\Delta_D|$, which goes to 0 whenever $\Delta_D \to \infty$. This property explains the proximity of the QAH region to the $J_S = 0$ line at large $|\Delta_D|$, since very weak exchange is then sufficient to induce a level crossing between the surface states.

Along the $\Delta_D = 0$ line, whose gaps are plotted in Fig. 3(b), each septuple layer is an isolated two-Dirac-cone two-dimensional electron system that contributes a quantum unit to the AHE when its exchange splitting strength exceeds $\Delta_S$. The isolated septuple layer Hamiltonian is

$$H_{SL} = \begin{pmatrix} m_t & v_D k_- & \Delta_S & 0 \\ v_D k_+ & -m_t & 0 & \Delta_S \\ \Delta_S & 0 & m_b & -v_D k_- \\ 0 & \Delta_S & -v_D k_+ & -m_b \end{pmatrix}, \quad (2)$$
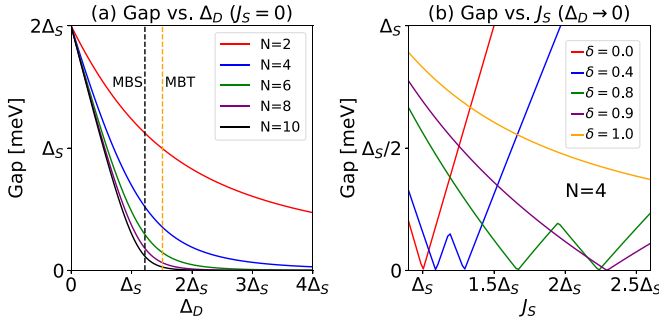
FIG. 3. Gaps vs hybridization between different septuple layers $\Delta_D$ and exchange splitting $J_S$. The quantized Hall conductance can change value only when gaps close. (a) Dependence on $\Delta_D$ at $J_S = 0$ for several thin film thicknesses. (b) Dependence on $J_S$ at $\Delta_D = 0$ for the four-layer thin film with the parallel surface magnetic configuration. Several different values of $\delta \equiv J_D/J_S$ are considered. For $\delta = 0$ and $\delta = 1$ no topological phase transition occurs as a function of $J_S$, in the former case because each septuple layer contributes the same sign of Hall conductivity as its spin magnetization, and in the latter case because topological transitions are absent. For other values of $\delta$ topological phase transitions occur between $C = 0$ and $C = 2$ states.

where $k_\pm \equiv k_y \pm i k_x$, and $m_{t/b}$ are top and bottom surface Dirac masses; here $t/b$ labels the two Dirac cones at the corresponding septuple layer. On the outside surfaces $m_{t/b}$ equals $\pm J_S$, whereas on the interior surfaces $m_{t/b}$ can equal $\pm(J_S + J_D)$ or $\pm(J_S - J_D)$ depending on the magnetic configuration. The eigenvalues of this Hamiltonian are

$$E = \pm \frac{1}{2}\sqrt{4v_D^2|k|^2 + \left(m_+ \pm \sqrt{m_-^2 + 4\Delta_S^2}\right)^2}, \quad (3)$$

where $|k| = \sqrt{k_x^2 + k_y^2}$ and $m_\pm \equiv m_t \pm m_b$. From Eq. (3) we see that the gaps are determined by the band energies at the two dimensional $\Gamma$ point. Using Eq. (3) it is easy to determine the Hall conductance contributed by each septuple layer along the $\Delta_D = 0$ line in any magnetic configuration. The $C = 2$ regions along the $\Delta_D = 0$ line in Fig. 2 appear when the surface septuple layers have entered QAH states, but the interior septuple layers still have zero Chern number.

The sensitivity of the phase diagram to $\delta$ is greatest at small $\Delta_D$. When $\delta$ and $\Delta_D$ both vanish, each septuple layer is driven into a QAH state when $J_S > \Delta_S$ with the Chern number sign depending on the direction of magnetic moment in that layer. It follows that for all perfectly compensated configurations the total Chern number vanishes in this limit. When $\delta \to 1$, a variety of different cases must be distinguished. Consider, for example, the top septuple layer when it is isolated by setting $\Delta_D \to 0$. For a $\uparrow\uparrow \cdots$ configurations the energies at $\Gamma$ are $E = (\pm J_S \pm \sqrt{J_S^2 + 4\Delta_S^2})/2$, whereas for a $\uparrow\downarrow$ $\cdots$ configurations $E = (\pm 3J_S \pm \sqrt{J_S^2 + 4\Delta_S^2})/2$. Similarly for an interior layers with a $\cdots \uparrow\uparrow\downarrow \cdots$ configuration $E = \pm J_S \pm \sqrt{J_S^2 + \Delta_S^2}$, whereas for $\cdots \uparrow\uparrow\uparrow \cdots$ configurations $E = \pm 2J_S \pm \Delta_S$. When level crossings occur as a function of $J_S$, the isolated septuple layer's contribution to the Hall conductivity changes from 0 to 1. The appearance or absence of QAH phases is easily determined by adding the contributions of all layers. These types of considerations explain the phase

transition points along $\Delta_D = 0$ lines in Figs. 2, 3(b), and 9 of Appendix B, which presents phase diagrams for $\delta = 0$ and $\delta = 1$.

## IV. DISCUSSION

The possibility of a QHE or a QAHE in noncollinear and in noncoplanar two-dimensional antiferromagnets has been explored [63–67] in previous theoretical studies of physically unrealistic toy models. In this paper, we have identified a practical route to achieve this unusual state by engineering the magnetic configurations of magnetic topological insulator thin films with perfectly compensated moments. The thinnest example is a four-layer structure with interior and exterior layer magnetizations having opposite orientations ($\uparrow\downarrow\downarrow\uparrow$), but many more configurations in this category appear in thicker films, as shown in the Appendix A, Fig. 6. The appearance or absence of a QAHE is dependent on the details of electronic structure and magnetic interactions. The dependence is described here in terms of the parameters of a simplified Dirac-cone model of the electronic structure with hybridization and exchange parameters $\Delta_S$, $\Delta_D$, $J_S$, and $J_D$ that predicts the phase diagrams in Fig. 2. It is possible to some extent to move through this phase diagram experimentally by varying the choice of chalcogen $X$ or the pnictide fraction $x$ in Mn(Bi$_x$Sb$_{1-x}$)$_2$X$_4$, by applying vertical strains, or by increasing temperature to reduce the effective exchange interaction strengths. For the case of MBT with $N \geqslant 6$ and the chosen parameters, all configurations with parallel surface (PS) layer magnetization have a QAH phase over a finite interval of temperature when thermal fluctuations in local moment orientations are assumed to decrease exchange interaction strengths [$m_i \to \xi m_i$ with $\xi \in (0, 1)$], as shown in Fig. 8 in Appendix B. For magnetic configurations with antiparallel surface magnetizations, no gap closings occur as a function of $\xi$, indicating that all remain in their $\xi = 0$ topologically trivial states (with zero Chern number) at any temperature.

A possible route to realize the magnetic configurations considered in this work is via cycling of magnetic fields. The resulting magnetic state of the thin film is dependent on magnetic anisotropy. The PS configurations of interest here are accessible when the magnetic anisotropy energy on the surface layers is sufficiently large. In a previous publication [62] we showed that the $N = 6$ PS magnetic configuration $M0'$ state in Fig. 1 (referred to there as $M0^*$) can be reached from the $M2'$ state when the ratio of the single-ion anisotropy coefficient $D$ to the interlayer exchange interactions $J$ is sufficiently larger than $0.23z$, where $z = 6$ is the interlayer Mn coordination. Specifically $D/zJ$ must be greater than 0.23, much larger than the $D/zJ$ ratio of bulk MnBi$_2$Te$_4$, which is approximately 0.13. (The bulk single-ion anisotropy energy of MnBi$_2$Te$_4$ $K \equiv DS^2$, where $S = 5/2$, is approximately 0.17 meV and corresponds to a value of $SD = 0.07$ meV [30,31,62]. The interlayer exchange interaction is $SJ = 0.088$ meV.) It seems likely, therefore, that the bulk anisotropy energy is insufficient to reach PS configurations in MnBi$_2$Te$_4$. On the other hand, just on the basis of symmetry, the surface layer magnetic anisotropy is likely to exceed the bulk value.
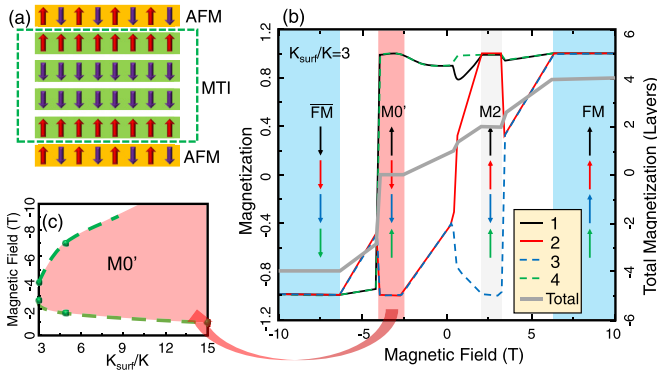
FIG. 4. The $N = 4$ parallel surface (PS) layer fully compensated collinear magnetic configurations can be realized by reversing the orientations of the top or bottom layers relative to the interior layers using exchange bias. The red and purple arrows in (a) represent moment orientations. (b) The $z$ component of total magnetization (gray line) and individual layer magnetizations (colored lines) that is predicted by classical Monte Carlo simulation of a $N = 4$ film at the temperature of 0.1 K. The effective surface layer magnetic anisotropy is 3 times the interior layer magnetic anisotropy. The shaded regions have collinear magnetic configurations, and the integer portion of the configuration label is the net number of aligned layers. The PS configuration is labeled $M0'$. (c) shows parameter range of surface magnetic anisotropy and magnetic field over which $N = 4$ PS states occur when the magnetization is swept toward negative values starting from $B = 10$ T.

Other strategies to realize PS magnetic configurations include finding related materials that have more favorable $D/zJ$ ratios, possibly $MnBi_4Te_7$ in which the interlayer coupling strength $J$ is much weaker, manipulating magnetic configurations using current-induced torques, and engineering effective anisotropy in the surface layers using exchange bias [68–70], as illustrated in Fig. 4(a). In principle it is possible to set the exchange bias by applying a large field near the Néel temperature of the insulating AFM exchange bias layer and then cooling down in field to well below the insulating AFM Néel temperature (below the so-called blocking temperature for exchange bias). For many exchange bias systems, the blocking temperature is much higher than the Neel temperature of MBT. Therefore, in the relevant temperature range here, the exchange bias on the top and bottom surfaces will then be basically independent of temperature. In this way we can tune the interlayer exchange coupling by tuning the temperature in a regime where the exchange bias remains fixed.

Normally, to estimate effective exchange bias field associated with an interfacial energy, we equate the energy from the field $H_{ex}$ with the energy obtained from the exchange bias. We denote the interfacial energy as $\epsilon$ (energy/unit area), the magnetization density as $M$, and the thickness of the exchange-biased magnet as $d$. That gives

$$\epsilon = H_{ex} \times M \times d. \tag{4}$$

The effective exchange bias is inversely proportional to the thickness $d$ of the magnetic layer. Typically, exchange bias interfacial energy is about 1 erg/cm$^2$ for real systems. When treat the surface layer of MBT as a ferromagnetic layer the

effective anisotropy field is about 1 T, $M = 2.62 \times 10^5 A/m$, and $d = 1.36$ nm. So to get a 3 T exchange bias field we need an interfacial energy density of 1 erg/cm$^2$. These parameters are reasonable to get a decent exchange bias.

This idea is quantified in Fig. 4(b), which plots the $\hat{z}$ component of total magnetization as a function of magnetic field, as the magnetic field is reversed from a saturating $B = 10$ T field. As illustrated in Fig. 4(c), the Chern insulator configuration with perfect spin moment compensation occurs over a wider and wider range of magnetic field as the surface layer magnetic anisotropy gets stronger and stronger. In order to get an exchange bias field, MBT may be exfoliated to an antiferromagnet such as $MnPS_3$ [71–73], FeO (111) surface, $Mn_3Ir$ [74], etc.

In summary, we predict that MTI thin film magnetization configurations with parallel surface layers will give rise to a QAHE even when the spin moments are perfectly compensated, and suggest a number of methods that can be employed to stabilize these configurations. This effect should become observable as MTI thin-film material quality improves.

## APPENDIX A: PERFECTLY COMPENSATED MAGNETIC CONFIGURATIONS

As discussed in the main text, the number of possible magnetic configurations with zero total magnetization awaiting exploration is thus $C(N, N/2)/2$, among which almost half of the magnetic configurations have parallel surface (PS) layers and the other half have antiparallel surface (APS) layers. In the limit of large $N$, the number of possible magnetic configurations is $C(N, N/2) \approx 2^N/\sqrt{\pi N/2}$ according to Stirling's approximation. Except for the all possible magnetic configurations of thin films with $N = 2, 4, 6$ shown in the main text, in Fig. 5 the compensated magnetic configurations for eight-layer thin film without time-reversal times inversion symmetry ($\mathcal{TI}$) are shown.

In Fig. 6 the number of possible magnetic states vs the thickness of thin films up to 16 layers are shown. The red curve shows the total number of PS magnetic configurations and blue curves are the number of APS magnetic configurations without $\mathcal{TI}$ symmetry. In the limit of $N \to \infty$ the ratio of PS configurations compared with the total number of magnetic configurations approaches $\sim$50%, as shown with the green dashed curve.
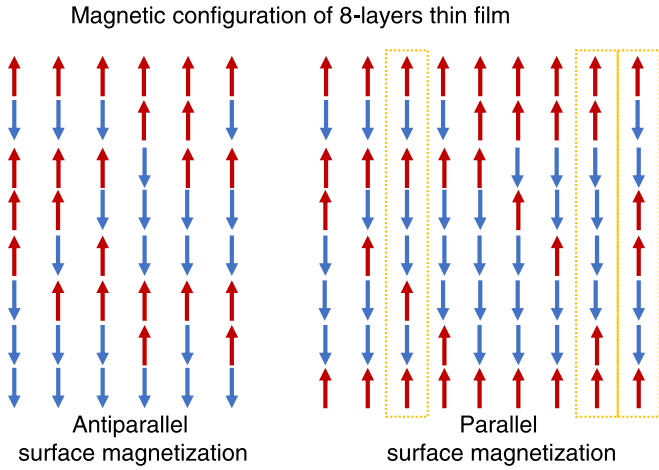
## Magnetic configuration of 8-layers thin film



FIG. 5. Magnetic configuration of eight-layer thin films without $\mathcal{TI}$ symmetry; each configuration has a time-reversal state. The APS configurations are shown in the left panel and the PS configurations are shown in the right panel. The magnetic configurations enclosed with a dashed rectangle have inversion symmetry.

## APPENDIX B: TOPOLOGICAL PHASE TRANSITION

For the case of MnBi$_2$Te$_4$ (MBT), we show that most of the PS magnetic configurations are in the QAH phase at low temperature; this is confirmed by the evolution of gaps vs the magnetization order parameter $\xi$, which is defined as

$$m_\xi = \xi m_i; \qquad (B1)$$

the mass gaps $m_i \equiv \sum_\alpha J_{i\alpha} M_\alpha$, where $\alpha$ is a layer label and $M_\alpha = \pm 1$ specifies the direction of magnetization on layer $\alpha$. $m_i$ is replaced with $m_\xi$ in which $\xi$ is varied from 0 to 1. When $\xi = 0$, the MBT thin films are trivial topological insulator thin films; there is a gap closing when $\xi$ is tuned from 0 to 1 continuously if a topological phase transition appears.

Gaps vs $\xi$ for MBT thin films with APS configurations and zero net magnetization are shown in Fig. 7, Figures 7(a)–7(d) are plots for thin films with thicknesses of 6–12 layers. From the plots we see that there is no gap closing when $\xi$ changes from 0 to 1, indicating that all APS magnetic configurations
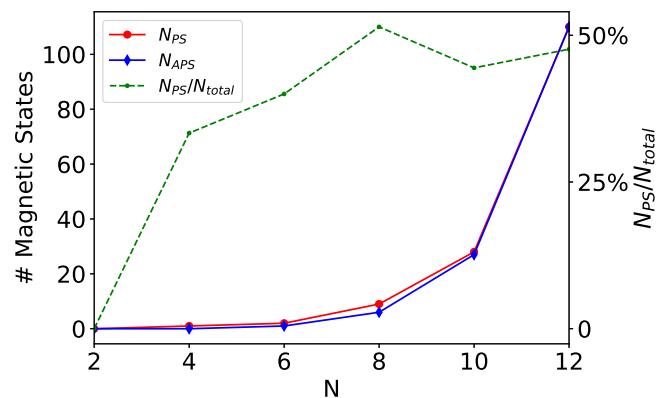


FIG. 6. Number of possible APS magnetic configurations without $\mathcal{TI}$ symmetry $N_{APS}$ (blue curve) and the number of PS magnetic configurations $N_{PS}$ (red curve). The fraction with PS configurations ($N_{PS}/N_{total}$) is plotted with a green dashed curve.
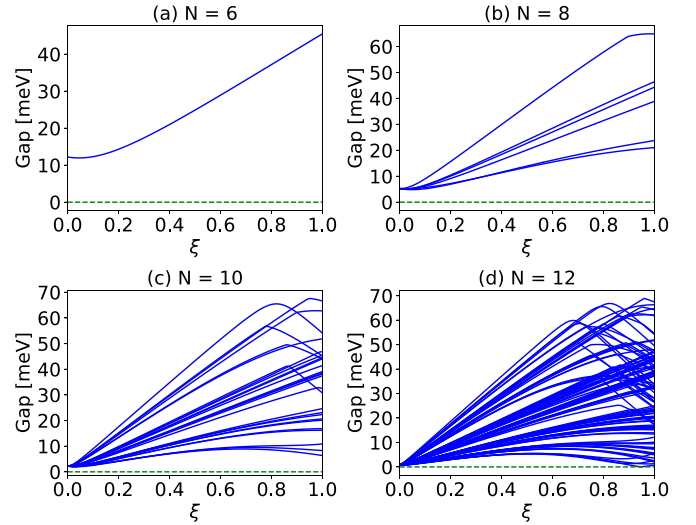


FIG. 7. Gaps vs $\xi$ for MBT thin films with antiparallel surface magnetization. All of magnetic configurations with zero net magnetization are shown, and (a)–(d) are plots for thin films with thicknesses of 6–12 layers.

are in the same topological phase as the topological insulator thin films with zero magnetizations, i.e., with zero Chern number.

In Fig. 8 the gaps of PS configurations vs $\xi$ for MBT thin films are plotted, where (a)–(d) are plots for thin films with thicknesses of 6–12 layers. When $\xi = 1$, configurations where the gap closes one time are in the QAH state while those where the gap closes two times are back to trivial insulator states. These plots show that at most PS configurations with zero net magnetization in MBT thin films are QAH states at $T = 0$, while the remaining ones are trivial insulators. However, for those configurations that have the gap closing
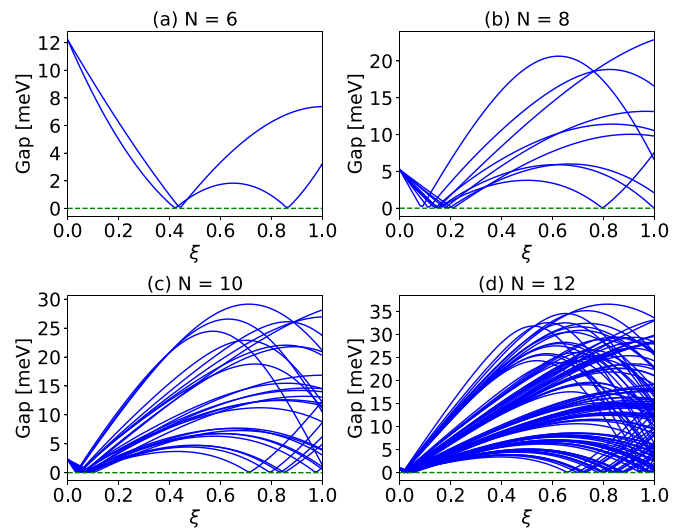


FIG. 8. Gaps vs $\xi$ for MBT thin films with parallel surface magnetization. (a)–(d) Plots for thin films with thicknesses of 6–12 layers. Configurations where gap closes one time are in QAH state while those the gap closes two times are back to trivial insulator states.
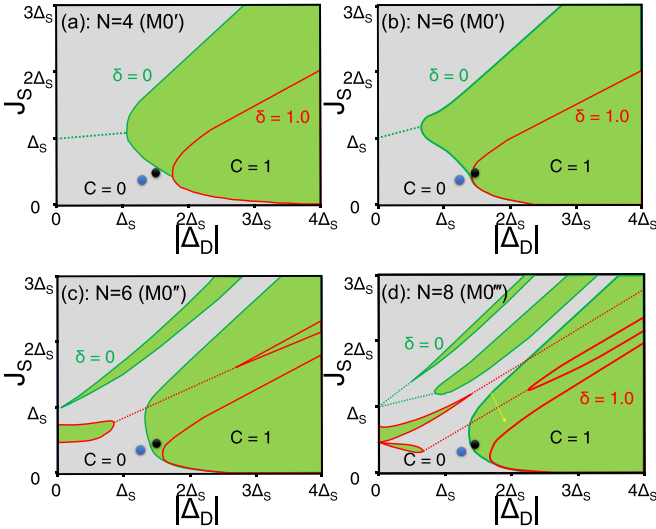
FIG. 9. Magnetic topological insulator thin film phase diagrams for a variety of fully compensated PS magnetic configurations with $\delta = 0$ and $\delta = 1$, which are defined in the main text. (a) $N = 4$ $M0'$ state; (b) $N = 6$ $M0'$ and (c) $N = 6$ $M0''$ state; (d) $N = 8$ $M0'''$ state with magnetic configuration ($\uparrow\downarrow\downarrow\downarrow\uparrow\uparrow\uparrow$); The light green regions of the phase diagram have Chern number magnitude $|C| = 1$, the grey regions have Chern number $C = 0$.

two times when $\xi$ changes from 0 to 1, there is a range of $\xi$ where all magnetic configurations are in QAH states. This indicates that the QAH states always appear at intermediate temperatures below the Néel temperature. This is strong evidence for the criteria that the QAH effect occurs in magnetic topological insulator thin films whenever the top and bottom surface layer magnetizations are parallel, independently of the magnetization configuration of interior layers.

Two-dimensional $|\Delta_D|/\Delta_S$-$J_S/\Delta_S$ topological phase diagrams calculated with $\delta \equiv J_D/J_S = 0$ (phase boundaries with green lines) and $\delta = 1$ (phase boundary with red lines) are
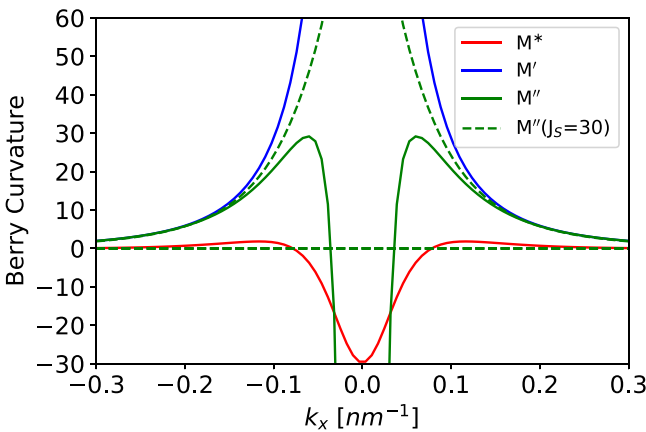


FIG. 10. Berry curvature vs $k_x$ for MBT thin films with thickness of $N = 6$ in various magnetic configurations. In the plot the $M'$ phase and M" phase with $J_S = 30$ meV are in topological phase with Chern number $C = 1$, while the other two cases have 0 Chern number. However, even with a total Chern number of zero, there is nonzero Berry curvature when the Fermi level is not in the gap.
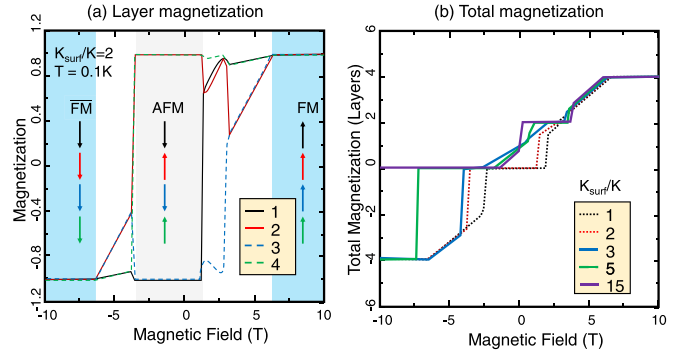


FIG. 11. Magnetizations of 4-layer thin film when the magnetic field is swept down from 10 T at the temperature of 0.1 K. (a) The magnetization in each layer with the surface magnetic anisotropy two times larger than the interior one. (b) The total magnetization when the surface magnetic anisotropy $K_{\text{surf}}$ changes from 1 to 15 times of the interior one $K$, the dashed curves contain states with compensated APS magnetic configurations, while the solid curves contain PS configurations.

shown in Fig. 9, with selected magnetic configurations discussed in the main text, i.e., several fully compensated PS magnetic configurations: Four-layer $M0'$, six-layer $M0'$ and $M0''$, and eight-layer $M0'''$. In the phase diagrams light green regions represent QAH states with Chern number $C = 1$ and the gray regions represent trivial insulators.

The Berry curvatures of the thin films with magnetic configurations shown in the main text are plotted in Fig. 10, where we use $N = 6$ thin films as the example for illustration.

## APPENDIX C: EXCHANGE BIAS

We performed Monte Carlo simulations for a four-layer thin film at temperatures of 0.1 and 2 K. In Fig. 11(a), the layer magnetizations for four-layer thin film with $K_{\text{surf}}/K = 2$ are
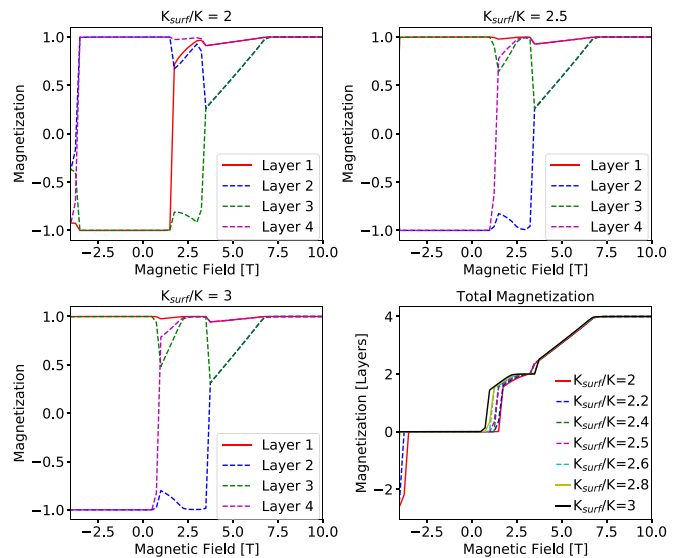


FIG. 12. Monte Carlo simulations of the four-layer thin films when the magnetic field is swept from 10 T, at a temperature of 2 K. (a)-(c) are the plots of layer magnetizations with the value of $K_{\text{surf}}/K$ as 2,2.5 and 3. (d) are the plots of total magnetizations.
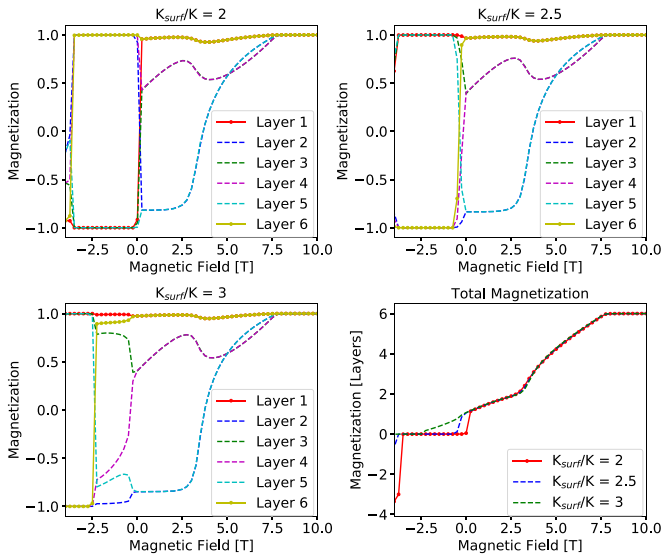
FIG. 13. Monte Carlo simulations of the six-layer thin films when the magnetic field is swept from 10 T, with the temperature of 2K. (a)–(c) Plots of layer magnetizations with the value of $K_{\mathrm{surf}}/K$ as 2, 2.5, and 3. (d) Plots of total magnetizations.

shown. Here $K_{\mathrm{surf}}$ is the magnetic anisotropy at the surface layers and $K$ is the magnetic anisotropy of the interior layers. The magnetizations of $K_{\mathrm{surf}}/K = 3$ are shown in the main text. The total magnetizations with several values of $K_{\mathrm{surf}}/K$ are shown in Fig. 11(b). For $K_{\mathrm{surf}}/K = 1$, 2, which are denoted as dashed curves, the magnetic configurations are APS when the total magnetizations are zero, while for other values of $K_{\mathrm{surf}}/K$ the antiferromagnetic states with zero total magnetizations are PS configurations.

When the temperature increases to 2 K, which actually does give rise to some small but perceptible thermal rounding, the compensated antiferromagnetic states with PS magnetic configurations disappear as shown in Fig. 12 for four-layer thin film. However, these PS magnetic configurations appear at 0.1 K, as shown in the main text.

For thicker films with the temperature of 2 K, such as the six-layer case, there are signatures of PS magnetic configurations with the value of $K_{\mathrm{surf}}/K = 3$. The layer magnetizations are plotted in Figs. 13(a)–13(c), which shows that $m_z$ have the same directions for layers 1, 3, and 6. The outermost layers are not completely parallel but have some canting. In Fig. 13(d) the total magnetizations are plotted.

[1] E. Hall, Am. J. Math. **2**, 287 (1879).

[2] E. H. Hall, London Edinburgh Dublin Philos. Mag. J. Sci. **12**, 157 (1881).

[3] N. Nagaosa, J. Sinova, S. Onoda, A. H. MacDonald, and N. P. Ong, Rev. Mod. Phys. **82**, 1539 (2010).

[4] K. van Klitzing, G. Dorda, and M. Pepper, Phys. Rev. Lett. **45**, 494 (1980).

[5] K. von Klitzing, Rev. Mod. Phys. **58**, 519 (1986).

[6] D. J. Thouless, M. Kohmoto, M. P. Nightingale, and M. den Nijs, Phys. Rev. Lett. **49**, 405 (1982).

[7] R. Karplus and J. M. Luttinger, Phys. Rev. **95**, 1154 (1954).

[8] J. Smit, Physica **21**, 877 (1955).

[9] J. Smit, Physica **24**, 39 (1958).

[10] L. Berger, Phys. Rev. B **2**, 4559 (1970).

[11] L. Šmejkal, A. H. MacDonald, J. Sinova, S. Nakatsuji, and T. Jungwirth, Nat. Rev. Mater. **7**, 482 (2022).

[12] H. Chen, Q. Niu, and A. H. MacDonald, Phys. Rev. Lett. **112**, 017205 (2014).

[13] S. Nakatsuji, N. Kiyohara, and T. Higo, Nature (London) **527**, 212 (2015).

[14] A. K. Nayak, J. E. Fischer, Y. Sun, B. Yan, J. Karel, A. C. Komarek, C. Shekhar, N. Kumar, W. Schnelle, J. Kübler *et al.*, Sci. Adv. **2**, e1501870 (2016).

[15] N. Kiyohara, T. Tomita, and S. Nakatsuji, Phys. Rev. Appl. **5**, 064009 (2016).

[16] T. Chen, T. Tomita, S. Minami, M. Fu, T. Koretsune, M. Kitatani, I. Muhammad, D. Nishio-Hamane, R. Ishii, F. Ishii *et al.*, Nat. Commun. **12**, 572 (2021).

[17] M. Naka, S. Hayami, H. Kusunose, Y. Yanagi, Y. Motome, and H. Seo, Phys. Rev. B **102**, 075112 (2020).

[18] H. Tsai, T. Higo, K. Kondou, T. Nomoto, A. Sakai, A. Kobayashi, T. Nakano, K. Yakushiji, R. Arita, S. Miwa *et al.*, Nature (London) **580**, 608 (2020).

[19] L. Šmejkal, R. González-Hernández, T. Jungwirth, and J. Sinova, Sci. Adv. **6**, eaaz8809(2020).

[20] Z. Feng, X. Zhou, L. Šmejkal, L. Wu, Z. Zhu, H. Guo, R. González-Hernández, X. Wang, H. Yan, P. Qin *et al.*, Nature Electronics **5**, 735 (2022).

[21] S. Hayami and H. Kusunose, Phys. Rev. B **103**, L180407 (2021).

[22] F. D. M. Haldane, Phys. Rev. Lett. **61**, 2015 (1988).

[23] C.-Z. Chang, J. Zhang, X. Feng, J. Shen, Z. Zhang, M. Guo, K. Li, Y. Ou, P. Wei, L.-L. Wang, Z.-Q. Ji, Y. Feng, S. Ji, X. Chen, J. Jia, X. Dai, Z. Fang, S.-C. Zhang, K. He, Y. Wang *et al.*, Science **340**, 167 (2013).

[24] R. Yu, W. Zhang, H.-J. Zhang, S.-C. Zhang, X. Dai, and Z. Fang, Science **329**, 61 (2010).

[25] M. M. Otrokov, I. P. Rusinov, M. Blanco-Rey, M. Hoffmann, A. Y. Vyazovskaya, S. V. Eremeev, A. Ernst, P. M. Echenique, A. Arnau, and E. V. Chulkov, Phys. Rev. Lett. **122**, 107202 (2019).

[26] C. Lei, S. Chen, and A. H. MacDonald, Proc. Natl. Acad. Sci. USA **117**, 27224 (2020).

[27] P. Wang, J. Ge, J. Li, Y. Liu, Y. Xu, and J. Wang, Innovation **2**, 100098 (2021).

[28] Y. Deng, Y. Yu, M. Z. Shi, Z. Guo, Z. Xu, J. Wang, X. H. Chen, and Y. Zhang, Science **367**, 895 (2020).

[29] S. Eremeev, M. Otrokov, and E. Chulkov, J. Alloys Compd. **709**, 172 (2017).

[30] J.-Q. Yan, Q. Zhang, T. Heitmann, Z. Huang, K. Y. Chen, J.-G. Cheng, W. Wu, D. Vaknin, B. C. Sales, and R. J. McQueeney, Phys. Rev. Mater. **3**, 064202 (2019).

[31] B. Li, J.-Q. Yan, D. M. Pajerowski, E. Gordon, A.-M. Nedić, Y. Sizyuk, L. Ke, P. P. Orth, D. Vaknin, and R. J. McQueeney, Phys. Rev. Lett. **124**, 167204 (2020).

[32] A. Zeugner, F. Nietschke, A. U. B. Wolter, S. Gaß, R. C. Vidal, T. R. F. Peixoto, D. Pohl, C. Damm, A. Lubk, R. Hentrich *et al.*, Chem. Mater. **31**, 2795 (2019).

[33] M. M. Otrokov, I. I. Klimovskikh, H. Bentmann, D. Estyunin, A. Zeugner, Z. S. Aliev, S. Gaß, A. U. B. Wolter, A. V. Koroleva, A. M. Shikin *et al.*, Nature (London) **576**, 416 (2019).

[34] M. M. Otrokov, T. V. Menshchikova, M. G. Vergniory, I. P. Rusinov, A. Yu Vyazovskaya, Y. M. Koroteev, G. Bihlmayer, A. Ernst, P. M. Echenique, A. Arnau *et al.*, 2D Mater. **4**, 025082 (2017).

[35] D. Zhang, M. Shi, T. Zhu, D. Xing, H. Zhang, and J. Wang, Phys. Rev. Lett. **122**, 206401 (2019).

[36] J. Li, Y. Li, S. Du, Z. Wang, B.-L. Gu, S.-C. Zhang, K. He, W. Duan, and Y. Xu, Sci. Adv. **5**, eaaw5685 (2019).

[37] S. Chowdhury, K. F. Garrity, and F. Tavazza, npj Comput. Mater. **5**, 33(2019).

[38] D. S. Lee, T.-H. Kim, C.-H. Park, C.-Y. Chung, Y. S. Lim, W.-S. Seo, and H.-H. Park, CrystEngComm **15**, 5532 (2013).

[39] E. D. L. Rienks, S. Wimmer, J. Sánchez-Barriga, O. Caha, P. S. Mandal, J. Růžička, A. Ney, H. Steiner, V. V. Volobuev, H. Groiss *et al.*, **576**, 423 (2019).

[40] S. H. Lee, Y. Zhu, Y. Wang, L. Miao, T. Pillsbury, H. Yi, S. Kempinger, J. Hu, C. A. Heikes, P. Quarterman, W. Ratcliff, J. A. Borchers, H. Zhang, X. Ke, D. Graf, N. Alem, C.-Z. Chang, N. Samarth, and Z. Mao, Phys. Rev. Res. **1**, 012011(R) (2019).

[41] C. Liu, Y. Wang, H. Li, Y. Wu, Y. Li, J. Li, K. He, Y. Xu, J. Zhang, and Y. Wang, Nat. Mater. **19**, 522 (2020).

[42] K. Y. Chen, B. S. Wang, J.-Q. Yan, D. S. Parker, J.-S. Zhou, Y. Uwatoko, and J.-G. Cheng, Phys. Rev. Mater. **3**, 094201 (2019).

[43] H. Deng, Z. Chen, A. Wołoś, M. Konczykowski, K. Sobczak, J. Sitnicka, I. V. Fedorchenko, J. Borysiuk, T. Heider, Ł. Pluciński *et al.*, Nat. Phys. **17**, 36 (2020).

[44] Y. Gong, J. Guo, J. Li, K. Zhu, M. Liao, X. Liu, Q. Zhang, L. Gu, L. Tang, X. Feng *et al.*, Chin. Phys. Lett. **36**, 076801 (2019).

[45] S. Zhang, R. Wang, X. Wang, B. Wei, B. Chen, H. Wang, G. Shi, F. Wang, B. Jia, Y. Ouyang *et al.*, Nano Lett. **20**, 709 (2020.

[46] H. Li, S.-Y. Gao, S.-F. Duan, Y.-F. Xu, K.-J. Zhu, S.-J. Tian, J.-C. Gao, W.-H. Fan, Z.-C. Rao, J.-R. Huang, J.-J. Li, D.-Y. Yan, Z.-T. Liu, W.-L. Liu, Y.-B. Huang, Y.-L. Li, Y. Liu, G.-B. Zhang, P. Zhang, T. Kondo *et al.*, Phys. Rev. X **9**, 041039 (2019).

[47] Y.-J. Hao, P. Liu, Y. Feng, X.-M. Ma, E. F. Schwier, M. Arita, S. Kumar, C. Hu, R. Lu, M. Zeng, Y. Wang, Z. Hao, H.-Y. Sun, K. Zhang, J. Mei, N. Ni, L. Wu, K. Shimada, C. Chen, Q. Liu *et al.*, Phys. Rev. X **9**, 041038 (2019).

[48] Y. J. Chen, L. X. Xu, J. H. Li, Y. W. Li, H. Y. Wang, C. F. Zhang, H. Li, Y. Wu, A. J. Liang, C. Chen, S. W. Jung, C. Cacho, Y. H. Mao, S. Liu, M. X. Wang, Y. F. Guo, Y. Xu, Z. K. Liu, L. X. Yang, and Y. L. Chen, Phys. Rev. X **9**, 041040 (2019).

[49] J. Ge, Y. Liu, J. Li, H. Li, T. Luo, Y. Wu, Y. Xu, and J. Wang, Natl. Sci. Rev. **7**, 1280 (2020).

[50] C. Hu, K. N. Gordon, P. Liu, J. Liu, X. Zhou, P. Hao, D. Narayan, E. Emmanouilidou, H. Sun, Y. Liu *et al.*, Nat. Commun. **11**, 97 (2020).

[51] L. Ding, C. Hu, F. Ye, E. Feng, N. Ni, and H. Cao, Phys. Rev. B **101**, 020412(R) (2020).

[52] P. Swatek, Y. Wu, L.-L. Wang, K. Lee, B. Schrunk, J. Yan, and A. Kaminski, Phys. Rev. B **101**, 161109(R) (2020).

[53] S. V. Eremeev, M. M. Otrokov, and E. V. Chulkov, Nano Lett. **18**, 6521 (2018).

[54] J. Wu, F. Liu, M. Sasase, K. Ienaga, Y. Obata, R. Yukawa, K. Horiba, H. Kumigashira, S. Okuma, T. Inoshita *et al.*, Sci. Adv. **5**, eaax9989 (2019).

[55] R. C. Vidal, A. Zeugner, J. I. Facio, R. Ray, M. H. Haghighi, A. U. B. Wolter, L. T. Corredor Bohorquez, F. Caglieris, S. Moser, T. Figgemeier, T. R. F. Peixoto, H. B. Vasili, M. Valvidares, S. Jung, C. Cacho, A. Alfonsov, K. Mehlawat, V. Kataev, C. Hess, M. Richter *et al.*, Phys. Rev. X **9**, 041065 (2019).

[56] I. I. Klimovskikh, M. M. Otrokov, D. Estyunin, S. V. Eremeev, S. O. Filnov, A. Koroleva, E. Shevchenko, V. Voroshnin, A. G. Rybkin, I. P. Rusinov *et al.*, npj Quantum Mater. **5**, 54 (2020).

[57] H. Sun, B. Xia, Z. Chen, Y. Zhang, P. Liu, Q. Yao, H. Tang, Y. Zhao, H. Xu, and Q. Liu, Phys. Rev. Lett. **123**, 096401 (2019).

[58] M. Gu, J. Li, H. Sun, Y. Zhao, C. Liu, J. Liu, and Q. Liu, Nat. Commun. **12**, 3524 (2021).

[59] S. Wimmer, J. Sánchez-Barriga, P. Küppers, A. Ney, E. Schierle, F. Freyse, O. Caha, J. Michalicka, M. Liebmann, D. Primetzhofer, M. Hoffmann, A. Ernst, M. M. Otrokov, G. Bihlmayer, E. Weschke, B. Lake, E. V. Chulkov, M. Morgenstern, G. Bauer, G. Springholz *et al.*, Adv. Mater. **33**, 2102935 (2021).

[60] I. Belopolski, S.-Y. Xu, N. Koirala, C. Liu, G. Bian, V. N. Strocov, G. Chang, M. Neupane, N. Alidoust, D. Sanchez, H. Zheng, V. Rogalev, T. Kim, N. C. Plumb, C. Chen, F. Bertran, P. Le Fèvre, A. Taleb-Ibrahimi, M.-C. Asensio *et al.*, Sci. Adv. **3**, e1501692(2017).

[61] C. Lei and A. H. MacDonald, Phys. Rev. Mater. **5**, L051201 (2021).

[62] C. Lei, O. Heinonen, A. H. MacDonald, and R. J. McQueeney, Phys. Rev. Mater. **5**, 064201 (2021).

[63] I. Martin and C. D. Batista, Phys. Rev. Lett. **101**, 156402 (2008).

[64] J. W. F. Venderbos, M. Daghofer, J. van den Brink, and S. Kumar, Phys. Rev. Lett. **109**, 166405 (2012).

[65] H. Ishizuka and Y. Motome, Phys. Rev. B **87**, 081105(R) (2013).

[66] G.-W. Chern, A. Rahmani, I. Martin, and C. D. Batista, Phys. Rev. B **90**, 241102(R) (2014).

[67] P. B. Ndiaye, A. Abbout, V. M. L. D. P. Goli, and A. Manchon, Phys. Rev. B **100**, 144440 (2019).

[68] S. Maat, K. Takano, S. S. P. Parkin, and E. E. Fullerton, Phys. Rev. Lett. **87**, 087202 (2001).

[69] J. Sort, V. Baltz, F. Garcia, B. Rodmacq, and B. Dieny, Phys. Rev. B **71**, 054411 (2005).

[70] F. Radu, R. Abrudan, I. Radu, D. Schmitz, and H. Zabel, Nat. Commun. **3**, 715 (2012).

[71] S. Lee, K.-Y. Choi, S. Lee, B. H. Park, and J.-G. Park, APL Mater. **4**, 086108 (2016).

[72] G. Long, H. Henck, M. Gibertini, D. Dumcenco, Z. Wang, T. Taniguchi, K. Watanabe, E. Giannini, and A. F. Morpurgo, Nano Lett. **20**, 2452 (2020).

[73] J. Yang, Y. Zhou, Q. Guo, Y. Dedkov, and E. Voloshina, RSC Adv. **10**, 851 (2020).

[74] S. Jenkins, R. W. Chantrell, and R. F. L. Evans, Phys. Rev. B **103**, 014424 (2021).